CHEMISTRY OF MATERIALS
Cite This: Chem. Mater. XXXX, XXX, XXX−XXX
Article
pubs.acs.org/cm

Huge Photostability Enhancement in Bismuth-Doped Methylammonium Lead Iodide Hybrid Perovskites by Light-Induced Transformation

Javier Bartolomé,[†,‡] Esteban Climent-Pascual,[†,§] Carlos Redondo-Obispo,[∥] Carlos Zaldo,[†] Ángel L. Álvarez,[∥] Alicia de Andrés,*[,†] and Carmen Coya*[,∥]

[†]Instituto de Ciencia de Materiales de Madrid, Consejo Superior de Investigaciones Científicas, C/Sor Juana Inés de la Cruz 3, 28049 Madrid, Spain

[‡]Departamento de Física de Materiales, Universidad Complutense de Madrid, Plaza Ciencias 1, 28040 Madrid, Spain

[§]Escuela Técnica Superior de Ingeniería Industrial, Universidad Politécnica de Madrid, C/José Gutiérrez Abascal 2, 28006 Madrid, Spain

[∥]Escuela Técnica Superior de Ingeniería de Telecomunicación (ETSIT), Universidad Rey Juan Carlos, C/Tulipán s/n, 28933 Móstoles, Spain

Supporting Information

ABSTRACT: The doping strategy of hybrid perovskites is being extensively explored not only for higher efficiency but also to overcome issues in photovoltaic materials such as self-degradation pathways in an ambient atmosphere or under visible irradiation. Here, BiI_3 is introduced in the synthesis of $MAPbI_3$ films (MA: $CH_3{-}NH_3^+$) to stabilize the material. Around 25% of nominal Bi^{3+} is accommodated in the perovskite structure, producing a shrinking of the unit cell and a small increase of the band gap. The presence of empty Bi gap states quenches the 770 nm red interband emission and results in a near-infrared emission at 1100 nm. However, high enough visible irradiation density induces a progressive segregation of Bi^{3+} out of the perovskite lattice and promotes the re-emergence of the red emission. This emission is blue-shifted, and its intensity increases strongly with time until it reaches a saturation value which remains stable in the transformed films for extremely high power densities, around 1000 times higher than for undoped samples. We propose that the underlying processes include the formation of BiI_3 and BiOI, probably at the surface of the crystals, hampering the usual decomposition pathways into PbI_2 and PbO_x for undoped $MAPbI_3$. These results provide a new path for obtaining highly stable materials which would allow an additional boost of hybrid perovskite-based optoelectronics.

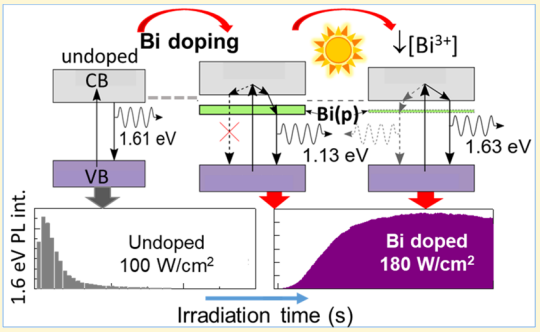

1. INTRODUCTION

Hybrid organic−inorganic perovskites solar cells have reached efficiencies as high as 22% for laboratory devices,[1,2] becoming comparable to established thin-film photovoltaic (PV) technologies, such as those based on CdTe and CIGS, in an astounding short time. Their predicted efficiency limit of 31%[3] along with their capability for cost-effective and low-temperature processing, such as spin coating and printing, have boosted the research on this subject in recent years. However, yet important challenges need to be overcome before reaching industrial maturity, especially the poor stability in ambient conditions of most standard $CH_3NH_3PbI_3$ ($MAPbI_3$). Moisture and O_2 are established as the major aging agents, causing the perovskite thin films to degrade in few days.[4] Recently, it has been demonstrated that laser illumination in ambient atmosphere of $MAPbI_3$ gives rise to the appearance of PbO_x phase and that moisture produces its decomposition to PbI_2.[5] In addition, despite the small amount present in the devices, Pb^{2+} is a toxic cation[6] not compatible with *green technologies*. This context has boosted the research activity aimed at replacing lead with *eco-friendly* alternatives through doping strategy. This is a challenging issue due to the demanding requirements for incorporating dopants that satisfy the octahedral coordination while keeping the stability of the perovskite structure, which can be estimated using the Goldschmidt's geometrical tolerance factor,[7] so that the same underlying crystal structure is maintained as well as good PV performance of the device.

In this context, tin-based perovskites and other alternative isovalent compositions, namely, $MASnI_3$, $MAPb_{1-x}Sn_xI_3$, $MASn_xPb_{1-x}Br_3$, $FA_{0.8}MA_{0.2}Sn_xPb_{1-x}I_3$, or $CsSnBr_xI_{3-x}$, have been indeed reported.[8−10] However, under ambient con-

Received: January 21, 2019
Revised: April 24, 2019
Published: April 26, 2019

DOI: 10.1021/acs.chemmater.9b00270
Chem. Mater. XXXX, XXX, XXX−XXX

ditions, Sn^{2+} is even less stable than Pb^{2+} and oxidizes easily to Sn^{4+}.[8] In addition, the devices based on Sn present much worse PV behavior than the lead halide perovskite.[8] Experiments with other isovalent cations such as Sr^{2+}, Cd^{2+}, and Ca^{2+} have resulted in an important deterioration of the PV performance,[11−13] except for the *also toxic* Hg-containing hybrid $MAPb_{1-x}Hg_xI_3$ salts, that exhibited improved solar cell performance at mercury amount around 10%.[14]

Another strategy is doping with heterovalent ions following the path of traditional semiconductors. Bi^{3+} doping is an interesting option because of the similar ionic radii of Bi^{3+}(VI) (1.03 Å) and Pb^{2+}(VI) (1.19 Å) and isoelectronic configurations of both ions. Wang et al. reported Bi-doped $MAPbI_3$ crystals which maintained the same crystal structure up to a molar 10 at. % of dopant in the precursor solution (1.6 at. % in the crystal) and exhibit increasing carrier lifetimes with Bi^{3+} doping and a 140 meV red shift of the absorption edge.[15] Bismuth-doped $MAPbI_3$ perovskites exhibiting near-infrared wide emission and a quenching of the red interband emission have also been reported.[16,17] Surprisingly, no changes in the crystal structure or lattice parameters neither in the wavelength of the red emission maximum are reported. Bismuth−silver halide double perovskite[18,19] and nonperovskite hybrid bismuth−iodide compounds, $MA_3Bi_2I_9$, have also been synthesized as crystals and thin films.[20,21] The latter material exhibits a very different crystal structure with poorer optoelectronic performances compared with $MAPbI_3$ but with higher tolerance against water and low toxicity so that it has been proposed as an absorber layer in tandem solar cells.[22]

In the present work, we report on Bi-doped $MAPbI_3$, $MAPbI_3$/(x at. %)Bi, thin films with nominally $0 < x < 33$. A detailed analysis of the X-ray diffraction (XRD) data is performed, obtaining important information about the impact of Bi doping on the film structure and growth habits and allowing the estimation of the actual doping. The combination of the structural information with results from optical spectroscopies indicates that Bi induces a small widening of the energy band gap and introduces electron traps below the conduction band that quenches the interband red emission and originates a near-infrared (NIR) emission. The stability of the films upon laser illumination was tested under ambient conditions, which are more stringent and closer to real operational conditions compared with the vacuum or N_2 atmosphere. At high irradiation power densities, the doped films undergo permanent modifications far away from the irradiated region, showing a recovered interband red emission with extraordinarily improved stability. The results are explained by the visible light-induced Bi ion segregation out of the perovskite lattice, promoting the re-emergence of the red interband emission, although blue-shifted and stable for extremely high power densities and periods of time compared with those of undoped samples. We propose a mechanism responsible for the observed effects where Bi migration and phase transformations, including BiI_3 and BiOI formation, are involved. This work sheds light in the understanding of the photochemical/physical mechanisms upon irradiation and provides a new path for the fabrication and processing of highly stable PV materials which would allow an additional boost of the hybrid perovskite-based optoelectronics.

2. EXPERIMENTAL SECTION

The synthesis of Bi-doped $MAPbI_3$ thin films is described in detail in the Supporting Information. Briefly, precursor solutions were prepared with amounts of MAI, PbI_2, and BiI_3 in dimethylformamide (DMF) according to the stoichiometric formula $MAPb_{1-1.5x}\square_{0.5x}Bi_xI_3$ (where □ stands for cation vacancy), x = 0, 8, 13, 18, and 33 at. % in the precursor solutions. These precursor solutions were used to obtain thin films by spin coating in an inert atmosphere. For simplicity, the obtained samples from the above solutions are named #0, #1, #2, #3, and #4 respectively. Table S1 provides a summary of the samples, including the nominal and incorporated compositions and the used nomenclature.

XRD data were collected at room temperature (RT) on a Bruker D8 FOCUS diffractometer (Cu Kα) over a 2θ range between 10 and 50° with a step size of 0.02°. The profile shape and lattice parameters were refined by the profile fitting (Le Bail fit) procedure using the FullProf program integrated in the WinPLOTR software.[23] Diffraction maxima were fitted with the Thompson−Cox−Hastings pseudo-Voigt function starting from the instrumental resolution values for the profile parameters. These starting profile parameters were obtained by fitting data obtained for alumina Standard Reference Material with smaller broadening effects and supplied by NIST. The background was characterized by using a 12-coefficient polynomial function. The average crystallite size and microstrain were evaluated using the Williamson−Hall method. Scanning electron microscopy (SEM) images were collected using a Philips XL30 ESEM scanning microscope with the secondary electrons detector. Energy-dispersive X-ray (EDX) compositional mapping was recorded in a Leica 440 Stereoscan SEM using a XFlash 4010 detector. To reduce the contribution from the substrate, the equipment was operated at low voltage (8 kV) and low current (1.5 nA). EDX fluorescence spectrometry (EDXFS): the chemical composition of the samples was studied by EDXFS carried out at the Spanish beamline BM25A SpLine at the European Synchrotron Research Facility (ESRF). Measurements were performed by means a 13-element Si(Li) solid-state fluorescence detector and a Si(111) monochromator, with an energy resolution of $\Delta E/E = 1.4 \times 10^{-4}$. The used excitation energy was 20 keV over an irradiated area of 1 mm^2. The energy-dispersive spectra collected during 1200 s for each sample were fitted using the PyMCA software.[24] Optical spectroscopies: the absorption spectra of the films were taken by a double-beam UV−vis Varian spectrophotometer (Cary 4000). The main optical transitions were obtained from the second derivative of the optical absorption spectra. The RT micro-photoluminescence (PL) spectra in the visible region (500−800 nm) were measured using the 488 nm excitation wavelength of an Ar^+ laser in backscattering geometry with an Olympus microscope and a Jobin-Yvon HR-460 monochromator coupled to a Peltier-cooled Synapse CCD. The light was collected from <1, 5, and 25 μm diameter spots (corresponding to ×100, ×20 and ×4 objectives). Different neutral optical filters were used to reduce the incident power on the samples (from 18 mW/cm^2 to 5500 W/cm^2 were used). Each point in the PL images corresponds to the integrated intensity in the 720−800 nm range of the spectrum corresponding to each position on the sample. For PL time evolution, whole spectra are obtained at different times and either the succession of the spectra (as a 2D image) or the integrated intensity of each spectrum in the 720−800 nm range are plotted versus time. PL spectra in the NIR (NIR PL) were acquired after excitation with a chopped Ar^+ laser at 488 nm (100 mW/cm^2) focused in 200 μm diameter spots with a Czerny Turner SPEX 0.34 m spectrometer and a 77 K cooled Ge photodiode connected to a lock-in amplifier. NIR PL time evolution was measured at 30 W/cm^2 incident power at 1100 nm with wide slits allowing ca. 40 nm spectral width. All NIR PL spectra were corrected by the spectral response of the experimental set-up. Lifetimes of NIR emission were measured by using a MOPO laser system tuned at 488 nm and detected with a Peltier-cooled NIR Hamamatsu photomultiplier plus a Tektronix model TDS 520 (500 MHz) oscilloscope.

DOI: 10.1021/acs.chemmater.9b00270
Chem. Mater. XXXX, XXX, XXX−XXX

3. RESULTS AND DISCUSSION

3.1. Morphology, Composition, and Structure. Precursor solutions ($MAPbI_3$, $MAPbI_3$/(8 at. %)Bi, $MAPbI_3$/(13 at. %)Bi, $MAPbI_3$/(18 at. %)Bi, and $MAPbI_3$/(33 at. %)Bi), named #0, #1, #2, #3, and #4, respectively, exhibit a reddish color, but cured films present a dark brown color, similar to the reference $MAPbI_3$, with a mirror-like and homogenous appearance (Figure S1). As shown below, sample #4 presents the formation of significant amounts of $MA_3Bi_2I_9$ secondary phase, and therefore, it will not be considered in the general discussion except for the trends in the XRD results with Bi incorporation. SEM images (Figure 1a) reveal that the

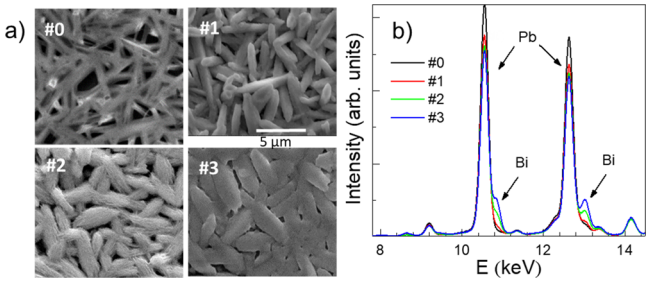

Figure 1. (a) SEM images of #0, #1, #2, and #3 thin films with the same magnification. (b) EDXFS spectra showing the main signals for Pb and Bi ions.

introduction of bismuth drastically changes the morphology of the films. The films show the formation of rod-like structures whose aspect ratio (length/width) decreases significantly with the increasing Bi content, mainly by increasing their width, leading to an increase in the volume of the grains and the density of the films. The profilometry measurements indicate that the thickness decreases as the amount of bismuth increases. For thin films obtained from precursor solutions, that is, (MAI + $[PbI_2]_{1-1.5x}$ + $[BiI_3]_x$) at a concentration of 25 wt % in anhydrous DMF (see Supporting Information), we obtain 345, 320, 290, and 280 nm for #0, #1, #2, and #3 thin films, respectively.

The Bi content within the samples was estimated by EDXFS (Figure 1b) of the thin films. The EDXFS spectra show that the bismuth content increases according to #1 < #2 < #3, however always below the nominal composition. Relative Bi/Pb ratios of 0.04, 0.10, and 0.14 were obtained for samples #1, #2, and #3, respectively. These values are smaller than the nominal Bi/Pb ratios of 0.09, 0.17, and 0.25, respectively, and correspond to approximately 45−58% of the nominal ones (Table S1). It is worth noting that these measurements account for the whole Bi content in the films which, as we shall see later, is different from that of substitutional Bi inside the $MAPbI_3$ perovskite.

The phase purity, symmetry, lattice parameters, average crystalline domain size, and microstrain of the samples were evaluated by means of XRD. Figure 2a,b shows these patterns for the five thin films (#0−#4).

The reflections have been indexed on the basis of the tetragonal *I*4*cm* space group proposed by Stoumpos et al. for $MAPbI_3$ single-crystal[8] who considered a polar tetragonal structural model, where the C−N bonds of the methylammonium cations are fixed parallel to the *c*-axis. XRD patterns for the pristine $MAPbI_3$ (#0) and for sample #1 indicate that pure *I*4*cm* tetragonal perovskite materials were obtained. However,

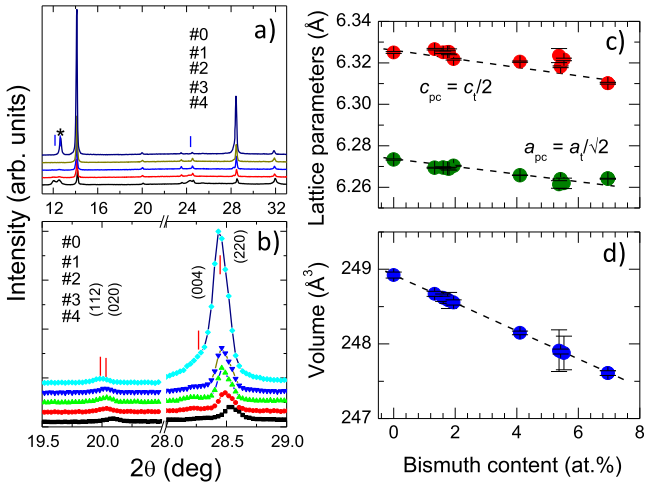

Figure 2. (a) XRD (Cu Kα_1/α_2) patterns of the films (#0−#4) at 298 K, the asterisk indicates the presence of PbI_2 for #0 film. (b) Details of two regions, indexed with the tetragonal *I*4*cm* space group, showing the large decrease of (220) intensity upon Bi doping. The red and blue vertical marks indicate the Bragg reflections of the $MAPbI_3$ and $MA_3Bi_2I_9$ phases, respectively. (c) Variation of the pseudocubic lattice parameters and (d) of the volume with bismuth content in the tetragonal Bi-doped $MAPbI_3$. The standard deviations are included. The dashed lines are guides to the eye.

the XRD patterns for the samples with higher nominal bismuth contents (#2−#4) revealed the presence of $MA_3Bi_2I_9$ (Figure 2a; blue vertical marks), reaching the maximum fraction for sample #4. The reflections corresponding to the zero-dimensional $MA_3Bi_2I_9$ phase were indexed to a $P6_3/mmc$ hexagonal cell.[25] Additional XRD patterns recorded at low angle (2θ < 10°, not shown) did not evidence other intermediate or hydrate phases.

The heterovalent substitution of the divalent cation Pb^{2+} for the trivalent cation Bi^{3+} induces the formation of cation vacancies (V_{MA} or V_{Pb}) and/or iodine interstitials (I_i). Anion interstitials in perovskites are usually difficult to accommodate because it is a compact structure, but such interstitials associated with undercoordinated lead sites (I vacancies) have been reported to be present at grain boundaries and surfaces for these halide perovskites.[26−28] Our XRD analysis shows that Bi^{3+} can be accommodated in the perovskite structure, but for high doping levels, an important fraction of the Bi promotes the formation of the lead-free $MA_3Bi_2I_9$ phase. It is important to note that only the undoped $MAPbI_3$ film exhibits the presence of a small amount of PbI_2 (Figure 2a; asterisk), usually observed in films. PbI_2 is not detected in any of the bismuth-doped films.

No variations in lattice parameters of the perovskite structure induced by Bi doping have been reported so far, probably related to the difficulty of effectively incorporating bismuth into the $MAPbI_3$ crystal structure. Here, we present the bismuth content dependence of the pseudocubic lattice parameters and cell volume, which is depicted in Figure 2c,d for a large number of films corresponding to different fabrication batches. The pseudocubic parameters are defined as $a_{pc} = a_t/\sqrt{2}$ and $c_{pc} = c_t/2$, and their values were obtained from the tetragonal lattice parameters (a_t and c_t) refined from the XRD data by the profile fitting method (Figure S2). The variations are small but clearly larger than the errors indicated in Figure 2c. In Figure S3, the cell volume is plotted versus the

DOI: 10.1021/acs.chemmater.9b00270
Chem. Mater. XXXX, XXX, XXX−XXX

nominal Bi content, while in Figure 2c,d we show the lattice parameters and volume as a function of an estimation of the substitutional bismuth content. Taking into account the differences in the valence state and ionic radii (Pb^{2+}(VI) = 1.19 Å and Bi^{3+}(VI) = 1.03 Å), it is possible to obtain a rough estimation of the Bi content inside the perovskite structure considering that the pseudocubic cell volume should decrease by about 0.20% every 1.10×10^{20} Bi atoms cm^{-3} (2.5 at. % Bi^{3+} at Pb^{2+} octahedral position) in the cell. As a first approximation, the possible effect of expected compensation defects (vacancies or interstitial sites) has not been considered in this assumption. In that way, the estimated concentration of substitutional Bi^{3+} at Pb^{2+} sites is 2, 4, 5, and 7 at. % for #1, #2, #3, and #4 films, respectively (Figure S3). Both lattice parameters and cell volume slightly decrease with the increasing bismuth content up to 7 at. %, which is a doping level much less than expected considering the nominal bismuth compositions (up to 33 at. % in the precursor solutions). This shows that there is a chemical phase separation for all of the prepared thin films, with only 20−25% of the nominal bismuth accommodated at the corner-sharing octahedra of the *I4cm* tetragonal perovskite. The remaining bismuth should be located at the isolated pairs of face-sharing octahedra in the lead-free phase $MA_3Bi_2I_9$ ($P6_3/mmc$) or be present in some spurious phases such as unreacted BiI_3 precursor, but the latter possibility was not observed in our XRD study. To better understand the impact of bismuth incorporation in the structure, both crystallite size and microstrain were estimated for each bismuth content using the dependence of fwhm × cos(θ) versus sin(θ) according to the Williamson−Hall procedure (Figure 3a).

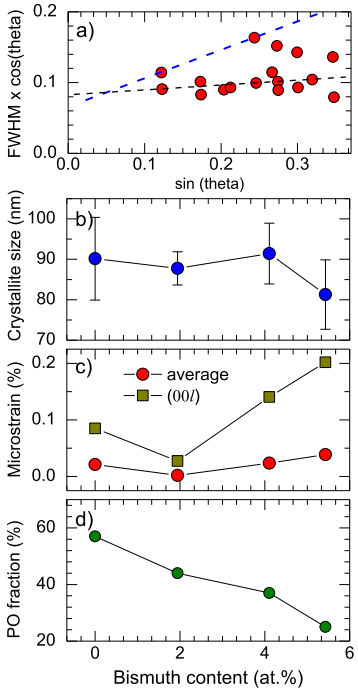

Figure 3. (a) Williamson−Hall plot for #3 film, black and blue dashed lines indicate the 00*l* (blue) and average *hkl* (black) fits. Bismuth content dependence of the average crystalline domain size (b), microstrains (c), and (110) PO fraction (d) for the tetragonal doped $MAPbI_3$ #0−#3 films.

This method allows for the simultaneous determination of the average crystalline domain size and possible effect of bismuth distribution inhomogeneities from the width of the diffraction maxima (the details of the procedure are described in the Supporting Information). The first result is that strain is almost negligible (Figure S4 and Table S2 in Supporting Information) and that the peak width is mainly due to the average crystal size that presents some variation upon doping (Figure 3b). Looking in more detail, it is possible to detect from the Williamson−Hall plots (blue dashed lines in Figures S4 and 3a) that, for high Bi content, the 00*l* reflections present higher strain values (Figure 3c). This can be explained considering a distribution of interplanar spacings for the (00*l*) planes due to a more marked inhomogeneity along *c*-axis upon bismuth doping, which could also be the cause for the higher data dispersion of *c*-lattice parameters in Figure 2c.

The almost constant crystallite size (~90 nm) obtained from XRD is not contradictory with the change in the aspect ratio of the grains observed with imaging techniques (as optical, SEM, or atomic force microscopy) because, in the first case, the size corresponds to the coherently diffracting domains within the grains. At higher doping levels, the estimated microstrain increases for the (00*l*) oriented grains and the crystallite size decreases slightly. However, the perovskite structure remains up to 7 at. % (maximum bismuth content, sample #4). Bi doping has a strong influence on the film morphology and also on its texture. As the bismuth content increases, the XRD patterns show that the ⟨110⟩ preferred orientation for the perovskite structure decreases (Figure 3d). The huge intensity decrease of *hh*0 peaks upon doping seen in Figure 2b can be explained by the reduction of the preferential orientation (PO) fraction from 57% for the undoped sample down to 25% for 5 at. % Bi-doped film (#3). This is probably related to the appearance of the $MA_3Bi_2I_9$ spurious phase for high nominal bismuth contents and to the disorder along the *c*-axis as Bi is introduced. Both combined events may contribute to the increase of the polycrystalline fraction in the films and also to the observed change in morphology.

3.2. Optical Band Gap. The optical absorption of the samples has been obtained in the 350−2500 nm (3.54−0.5 eV) range (Figure 4). The absorbance spectrum of $MAPbI_3$ (#0) agrees with the published results, with an absorption coefficient around 10^5 cm^{-1} (Figure S5a).[29] Note that the

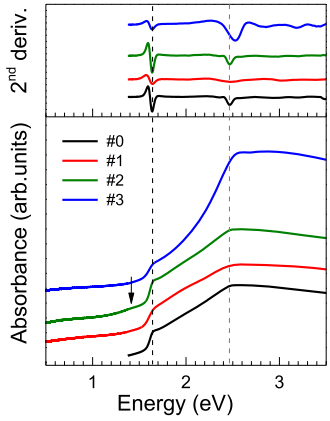

Figure 4. Absorbance and its second derivative (upper panel) for each thin film: #0 black solid line; #1, red solid line; #2, green solid line; #3 blue solid line.

DOI: 10.1021/acs.chemmater.9b00270
Chem. Mater. XXXX, XXX, XXX−XXX

surface roughness of the samples can lead to large errors in the identification of the optical band gap E_g.

In fact, typical Tauc plots (Figure S5b) also have been demonstrated to miscalculate E_g and cannot in general be straightforwardly applied to materials with complex band structures, even though it is a useful tool to qualitatively observe changes in the gap or the character of the transition.[29−31] To estimate the optical transition energies, we have employed the second derivatives of the absorbance spectra because the minima correspond to absorption maxima and therefore to electronic transitions.[32] The second derivatives of the optical absorption spectra measured for the films #0−#3 exhibit two local minima, one at 1.6 eV and the second in the range of 2.4−2.5 eV, corresponding to direct semiconductor-type transitions at the R and M points in the pseudocubic Brillouin zone, respectively.[29,33] The same values found for the first main optical transition at 1.6 eV for #0 (±0.03 eV), #1 (±0.05 eV), #2 (±0.05 eV), and #3 (±0.06 eV) [in parenthesis the errors estimated from the full width at half-maximum (fwhm) of the second derivatives] indicates that Bi introduction does not induce appreciable changes on E_g. However, a weak band around 1.4 eV (arrow in Figure 4) may be associated with Bi empty states. Thus, up to 18 at. % in the precursor solution (5 at. % Bi in the perovskite), the introduction of Bi does not lead to noticeable changes in the E_g values compared with undoped $MAPbI_3$, and therefore, no changes in the visible emission characteristics are anticipated.

3.3. Photoluminescence. The PL emission in undoped $MAPbI_3$ has been extensively studied and reported to exhibit a complex evolution with illumination power and time.[27] It is also dependent on the ambient conditions, especially sensitive to humidity and oxygen, and evolves differently according to the nature of the substrate on which the $MAPbI_3$ film has been grown by favoring the formation of different state traps in the material.[5,34] The presence of defects, particularly halide vacancies, photoinduced defects and, in general, trap states and their evolution with the previously described factors, play an important role in the nonradiative processes influencing the recombination dynamics.[35,36] deQuilettes et al.[26] showed that major PL changes in vacuum are related to field assisted photohalide migration that gives rise to a decrease in the density of trap states, indicating also that other complex mass transport mechanisms may simultaneously occur.

To study the behavior and stability of the Bi-doped films upon irradiation under ambient conditions, their PL was measured for different power densities with a 488 nm laser. For comparison purposes, the evolution of the undoped $MAPbI_3$ film (#0) was measured under the same conditions (Figure S6a−e). The undoped film shows the expected red PL at 770 nm whose intensity increases at different rates depending on the power density (Figures 5a,b and S6d). At low power densities (18 mW/cm^2) the emission is stabilized after 300 s. The PL enhancement is related to the reduction of the traps density that, according to ref 26, is induced by the migration of the iodine out of the irradiated region. Increasing power density increases the rate at which the maximum intensity is reached but also induces an irreversible degradation in the samples because of the gradual transformation to PbO_x as can be evidenced through its Raman spectrum.[5] For 180 mW/cm^2, the degradation starts after only 100 s (Figure 5b). It is important to note that the emission wavelength maximum does not change (770 nm, 1.61 eV) for the undoped sample in spite of the large changes occurring in the whole process.

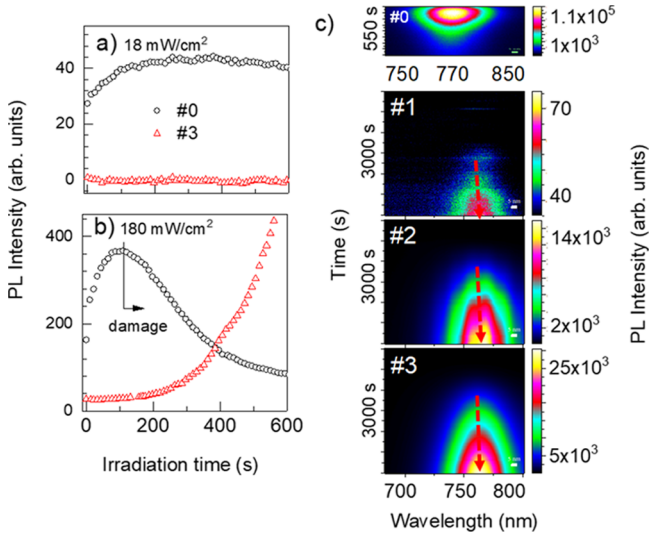

Figure 5. Evolution of PL intensity (integrated in the range 720−800 nm) with irradiation time for (a) 18 mW/cm^2 and (b) 180 mW/cm^2 incident power (488 nm, 25 μm spot) for the undoped (#0, black circles) and Bi-doped (#3, red triangles) $MAPbI_3$ films. (c) PL spectra evolution with time up to 3000 s for #1, #2, and #3 films under irradiation with 180 W/cm^2 (5 μm spot). Note the very different intensity scales for the three samples. The evolution of #0 film has also been included for comparison. Because of the fast degradation of this sample, the irradiation power was limited to 100 W/cm^2 and the time scale is reduced to 550 s.

The phenomenology for the Bi-doped samples is drastically different. The 1.61 eV (770 nm) PL is initially absent in all cases (Figure S6f). In contrast, a NIR emission peaking around 1.13 eV (1100 nm), plotted in Figure S7a, is detected for the #1−#3 samples exhibiting equal average lifetime (Figure S7b). This NIR PL is absent for undoped samples. According to calculations, the incorporation of Bi^{3+} introduces empty states in the gap relatively close to the conduction band, at around 1.1 eV from the valence band.[37] These empty states act as electron traps and would be responsible for the quenching of the red luminescence and originate the observed NIR emission.

Interestingly after irradiation of Bi-doped samples for some time, which depends on the Bi doping and on the optical power density on the sample, the red emission band emerges. In contrast to undoped $MAPbI_3$ thin film, the Bi-doped samples do not present any visible emission even after several minutes illuminated at 18 mW/cm^2 (Figure 5a). However, increasing power density (e.g., 180 mW/cm^2 in Figure 5b) induces the emergence of an initially extremely weak PL band at slightly higher energy, around ∼1.65 eV (745−750 nm), than that of the undoped film, 1.61 eV (770 nm). The intensity of this red band increases noticeably with irradiation time and its wavelength shifts to larger values up to 1.63 eV (760 nm) but never reaching that corresponding to undoped $MAPbI_3$ (Figure S6f). Figure 5c illustrates the general behavior of the PL emission of Bi-doped samples at high irradiation density (180 W/cm^2) during 3000 s. The maximum reached intensity increases drastically with Bi content, although never achieving the maximum values obtained in the undoped films, and presents almost identical final wavelength for all samples, 760 nm. The small shift to higher energies of the emission band (0.02−0.04 eV) is compatible with the unchanged band gap measured by absorption spectroscopy considering its un-

DOI: 10.1021/acs.chemmater.9b00270
Chem. Mater. XXXX, XXX, XXX−XXX

certainty (1.61 ± 0.05 eV) (Figure 4); however, it disagrees with the reported band gap red shift of Bi-doped perovskites.[15−17] This red shift has nevertheless been very recently refuted due to problems related to reduced transmittance of the films and to the presence of defect states,[37,38] in agreement to our observations. The blue shift of the emission band indicates a very small increase of the gap which can be explained by the structural impact of Bi incorporation into the perovskite lattice. Indeed, as shown in Figure 2, the lattice parameters and unit cell volume decrease upon doping which may produce an increase of the band gap and therefore of the interband emission energy. An increase of the band gap upon volume reduction also happens in the tetragonal to orthorhombic transition at low temperature in $MAPbI_3$.[39−41]

Figure 6b shows a top view cross-polarized optical image of sample #3 after being irradiated for 4600 s with 180 W/cm^2 power density (1000 times higher than in Figure 5b). The blue circle indicates the size of the laser spot (25 μm diameter, ×4 objective). The image (obtained with ×20 objective, 5 μm laser spot) shows a large area of transformed material composed of a dark region centered at the laser spot surrounded by a brown-yellow ring and, farther from the center, a concentric area of brighter grains. The PL intensity versus time during this process is plotted in Figure 6a showing first the rapid raise (up to around 1000 s) and then a slow degradation.

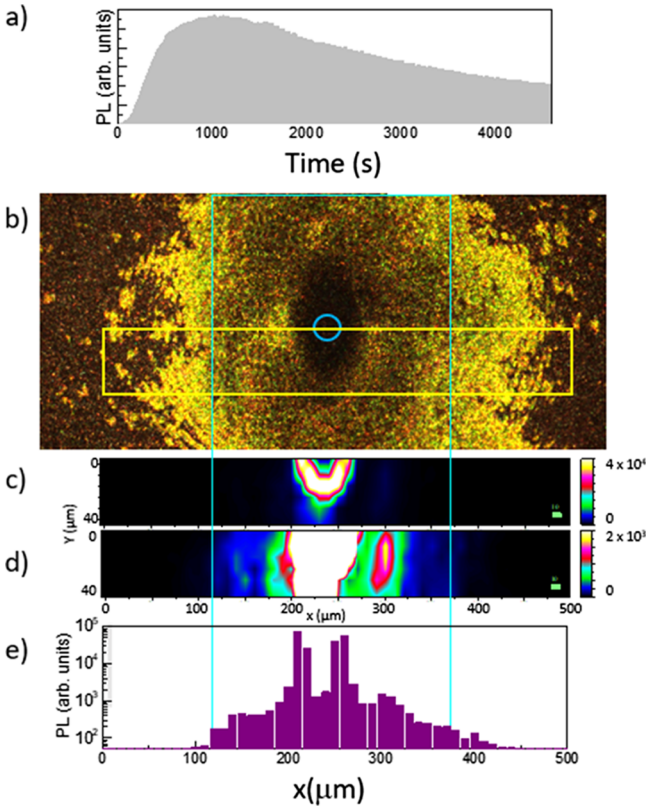

Figure 6. (a) Time evolution of the PL intensity (integrated in the range 720−800 nm) under 180 W/cm^2 irradiation of #3 $MAPbI_3$/Bi film; (b) cross-polarized optical image after 76 min illumination, the blue circle indicates the laser spot (25 μm); (c,d) PL images of the region indicated with a yellow rectangle in (b) with different intensity scales (40 000 and 2000) and (e) profile of the integrated intensity (in the range 720−800 nm) along the upper edge of the yellow rectangle in logarithmic scale (10^2 to 10^5).

After the transformation, the red PL was checked again in the region of the sample indicated with a yellow rectangle (500 μm × 40 μm) using a ×20 objective (5 μm diameter spot) and a lower power density (100 W/cm^2) to reduce the alteration of the sample by this second measurement (note that the measure time is now short: 2.5 s per point). Figure 6c−e shows the PL intensity map with two different scales and the corresponding horizontal profile along the top of the PL images, in logarithmic scale. Directly at the location of the laser spot (blue circle in Figure 6b, 25 μm diameter), the intensity is depleted due to the degradation of the sample over time (Figure 6a); however, the surrounding area, comprising a ring with an outer diameter of ∼70 μm (dark central region in the cross-polarized image) shows a very high intensity. In fact, the enhancement of the PL signal extends much farther, with a significant PL intensity observed in a region of around 300 μm (blue rectangle in Figure 6), corresponding to the brown-yellow ring in the cross-polarized image. Note that bright isolated grains are observed, most probably suggesting that the whole grain is involved in the transformation. This is consistent with the discontinuous evolution (steps) of the first stages of PL with time (Figure S8). The brighter aspect in the cross-polarized images is related to the ability of the sample to depolarize the incident white light, revealing that transformations are occurring very far from the initial laser spot and that these are maintained after switching off the laser. These results strongly suggest that ion migration is involved in the process.

The observed trends can be explained with a model based on the segregation of Bi out of the perovskite lattice upon irradiation and its consequence on the $MAPbI_3$ cell volume. Figure 7 sketches the processes occurring for Bi-doped samples showing the $MAPbI_3$ unit cell volume decrease upon the

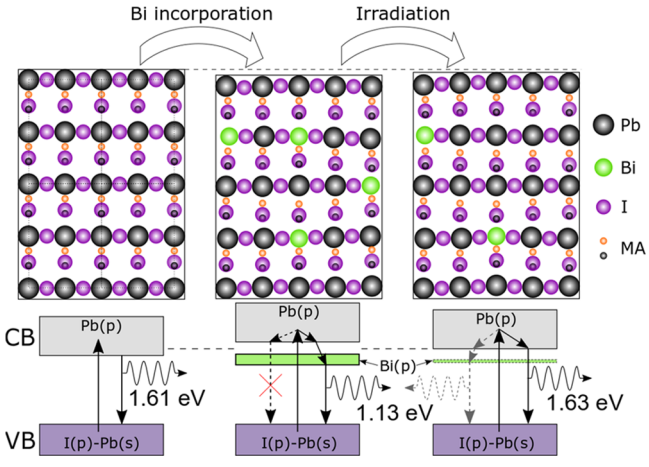

Figure 7. Schematic of the variation of the $MAPbI_3$ cell volume upon Bi doping and its influence on the optical properties. The incorporation of substitutional Bi^{3+} (green spheres) decreases the cell volume of the $MAPbI_3$, increasing its band gap. The Bi ions introduce empty states inside the band gap responsible for the NIR emission and band-to-band emission quenching. During photo-irradiation, the migration of Bi is activated. The decrease in the Bi content causes the partial recovery of the original cell volume and band gap, while reducing the amount of accessible states in the defect band, allowing the interband process to become dominant. The possible defects induced by heterovalent doping are not shown.

DOI: 10.1021/acs.chemmater.9b00270
Chem. Mater. XXXX, XXX, XXX−XXX

incorporation of substitutional Bi^{3+} and consequent band gap widening. The Bi states inside the band gap are responsible for emergence of the NIR emission at 1.13 eV which competes with usual red emission causing it to quench. However, during photoirradiation at high enough power densities, the segregation of Bi is activated by its migration out of the nanocrystallites (~90 nm) toward their surface, decreasing the Bi content inside the $MAPbI_3$ crystal down to a certain value, common for all doped samples.

This reduction of Bi doping causes the partial recovery of the original cell volume and band gap (still slightly smaller/larger than original values, respectively), while reducing the amount of accessible states in the defect band so that the interband radiative recombination process is recovered. As a consequence, the red emission wavelength is shifted from the extremely weak 1.65 eV (750 nm) emission to a much more intense emission around 1.63 eV (760 nm) and, in parallel, the intensity of the NIR emission at 1100 nm decreases (Figure 8a). Heavy cation mobility, such as Pb^{2+} in alkali halides, has

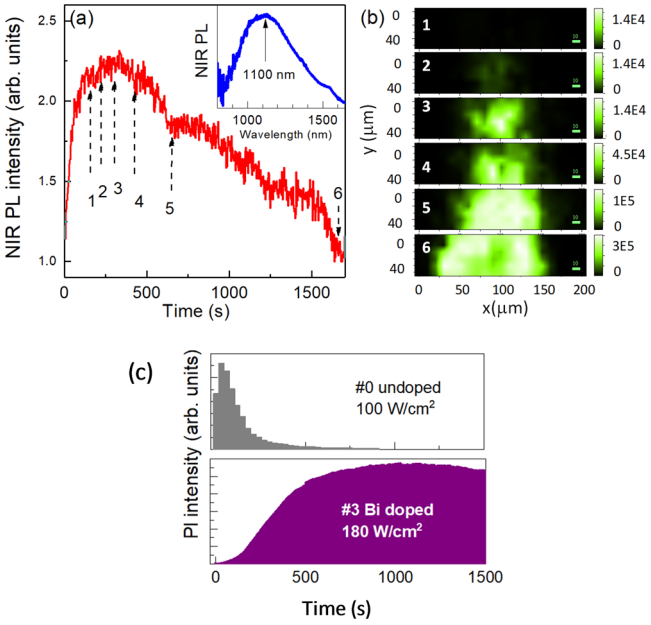

Figure 8. (a) Time dependence of the 1100 nm NIR PL band (inset) for film #3 upon illumination at 30 W/cm^2 (red line) and (b) PL images of the 770 nm band obtained in the same area, at times indicated by arrows in (a) showing the huge intensity increase (note also the increased intensity scales from 1 to 6) while NIR PL intensity declines. (c) Integrated intensity evolution in the 720−800 nm range with illumination time of undoped, #0, and Bi-doped film #3, for 100 and 180 W/cm^2, respectively.

been reported to be possible because of the presence of cation vacancies and temperature.[42] While a certain degree of local heating can be expected at the laser spot for high power densities, here it has been ruled out as the main driving force for Bi^{3+} migration: one of the samples (#3 film) was heated at increasingly higher temperatures in an ambient atmosphere (same conditions as in the irradiation experiments) and its PL was measured using low power densities to avoid further transformation with the laser. However, the huge increase in PL intensity was not detected at any measured temperature. Moreover, at around 120 °C, the film degraded, its color changed (see Figure S10), and the 770 nm PL was totally lost, and PL can no more be induced by laser irradiation.

A remarkable aspect of these Bi-doped $MAPbI_3$ films is that the resulting materials after illumination are extraordinarily resistant to further light modifications. The evolution of the PL intensities with illumination time at high power densities are plotted in Figure 8b,c for the undoped $MAPbI_3$, #0, and Bi-doped #3 films. While the degradation of the undoped film, #0, begins only after 30 s, in Bi-doped #3 film, once the transformation has occurred, the maximum intensity is stable at least for 1000 s. Film #3 has been tested with laser densities up to 2500 W/cm^2 after the local transformation. The intensity is maintained for some time, at least 30 s, up to the higher densities while in undoped film, at the laser spot, a hole in the film is immediately formed.

We propose a possible mechanism to explain this outstanding increased stability as well as the strong dependence of the maximum luminescence intensity on the initial Bi doping of these samples. Assuming that the final Bi content inside the illuminated region is similar for all of the doped samples, as proposed, the sole segregation of Bi as, for example, metallic Bi^0 should lead to similar maximum luminescence intensities independent of the initial Bi content, contrary to our observations. However, Bi can also be segregated as rhombohedral BiI_3, capturing three iodine ions either from the $MAPbI_3$ lattice or from residual PbI_2 as follows

$$Bi_{Pb}^{\bullet} + 3I_i' \xrightarrow{\text{irradiation}} V_{Pb}'' + BiI_3 \quad (1)$$

$$Bi_{Pb}^{\bullet} + I_i' + PbI_2 \xrightarrow{\text{irradiation}} Pb_{Pb}^{\times} + BiI_3 \quad (2)$$

$$Bi_{Pb}^{\bullet} \xrightarrow{\text{irradiation}} V_{Pb}'' + 3V_I^{\bullet} + BiI_3 \quad (3)$$

$$Bi_{Pb}^{\bullet} + 2PbI_2 + V_{Pb}'' + V_I^{\bullet} + MA_{MA}^{\times} \xrightarrow{\text{irradiation}} Pb_{Pb}^{\times} + MAPbI_3 + BiI_3 \quad (4)$$

The Kröger−Vink notation has been used here, where •, ′, × (positive, negative, or neutral) indicates the charge of the given defect in comparison to that of the atomic position it occupies. Reactions 1 and 2 are mediated by iodine interstitials (I_i), while reactions 3 and 4 involve iodine vacancies (V_I). Reaction 3 is very unlikely because it involves the creation of four different vacancies in the material. Reactions 1, 2, and 4 on the other hand involve either the annihilation of I_i, which is associated with deep trap states[43,44] or the decomposition of PbI_2 secondary phase. Both species are expected to negatively affect the luminescence of pure $MAPbI_3$. The existence of iodine interstitials is still subject of debate because the tight packaging of the perovskite structure usually hinders its formation because of the steric impediment. However, some theoretical works have estimated I_i formation energies which are low enough to allow a significant presence of this kind of defect,[28] while the homogenization and enhancement of the PL intensity upon light illumination (so called light soaking) have been attributed to I_i migration and redistribution.[26] Both reactions 1 and 2 and reaction 4 would lead to an improvement of the $MAPbI_3$ structure and subsequent PL emission properties which would depend on the initial Bi content, while the presence of residual Bi doping will limit the maximum intensity below the pristine $MAPbI_3$, as observed. This process can also explain the extraordinary stability under irradiation of the Bi/$MAPbI_3$ films compared with the undoped samples because BiI_3 formation and its subsequent oxidation to tetragonal BiOI[45] would compete with the

DOI: 10.1021/acs.chemmater.9b00270
Chem. Mater. XXXX, XXX, XXX−XXX

formation processes of PbI_2 and PbO_x phases during the degradation of pure $MAPbI_3$.[5] The here observed PL band at 1.63 eV cannot be associated with BiI_3 because this compound presents a weak PL emission above 1.8 eV.

The formation of rhombohedral BiI_3 and of BiOI during irradiation is difficult to assess by macroscopic techniques such as XRD because of the small and highly localized region where the transformation is produced; however, BiI_3 is known to be a birefringent material,[46] which could explain the bright ring around the laser spot observed in the cross-polarized image of Figure 6b, not detectable in nonpolarized images (Supporting Information Figure S9). The darker central region in the cross-polarized images is most probably the result of the transformation of BiI_3 into BiOI upon irradiation. This transformation has been observed when recording Raman spectra of BiI_3 powder: the BiI_3 Raman spectrum was not detected at all during the measurements, whereas a peak around 147 cm^{-1}, characteristic of BiOI,[47] was obtained instead. This peak first increases with successive measurements and then is stabilized (Figure S11) while no PL signal is detected. The light-induced transformation of BiI_3 into BiOI should lead to a decrease in the amount on I in the darker central spot, as confirmed by EDX compositional mappings (see Figure S12), by the sublimation of highly volatile I_2 molecules, thus decreasing the global content of I in the irradiated area. On the contrary, the Bi content remains constant because Bi is segregated toward the crystallite surfaces within the physical grains where it transforms into BiI_3 and BiOI.

4. CONCLUSIONS

In summary, we report on novel effects induced by heterovalent doping of $MAPbI_3$ with Bi^{3+} not observed so far. Bi doping has a strong influence on the film morphology, reducing the aspect ratio (length/width) of the rods and increasing the apparent density. XRD analysis shows that only a fraction around 25% of the Bi^{3+} present in the solution is accommodated in the perovskite structure. The tetragonal structure remains stable at least up to 7 at. % Bi incorporation with a reduction of the lattice parameters that is used to estimate the Bi^{3+} fraction at Pb^{2+} sites. Bi produces an important reduction of the (*hh*0) preferred orientation from 57 to 25% from undoped to doped films while the crystal domain size is almost unchanged. At doping levels >4 at. %, the crystallite size decreases slightly and the obtained microstrain increases for the (00*l*) grains probably associated with a larger distribution of *d*-spacing for (00*l*) planes because of higher inhomogeneity along *c*-axis upon bismuth incorporation.

Regarding optical properties, Bi introduction in the $MAPbI_3$ lattice only slightly increases the main optical gap; however, for the PL properties, the phenomenology for the Bi-doped samples is drastically different from that of $MAPbI_3$. Initially, the typical red band-to-band transition around 1.61 eV nm is totally quenched upon doping while a NIR emission at 1.13 eV is detected because of the Bi 6p empty states below the conduction band that act as electron traps. However, for high power irradiation densities, the red emission band raises with time, at a rate which is dependent on irradiation power density and Bi content. The observed trends can be explained using a model based on the migration of Bi^{3+} out of the perovskite lattice upon irradiation and its effect on the $MAPbI_3$ cell volume and band gap energy. Visible light fosters the progressive migration of Bi ions out of the perovskite lattice, thus allowing the emergence of the band-to-band emission that is blue-shifted compared with undoped films because of the band gap increase related to the reduction of the unit cell volume. The red band intensity strongly increases with time and progressively shifts up to 760 nm (1.63 eV) because of the migration of Bi out of the perovskite lattice, thus reducing again the band gap at a value however larger than that of undoped samples (1.61 eV). The radiation produces modifications in the film that are observable in cross-polarized optical images long time after the radiation is switched off and over an extension more than 10 times the laser spot size. Another remarkable aspect of these Bi-doped $MAPbI_3$ films is that the resulting material after illumination is extraordinarily resistant to light modifications, being stable for extremely high power densities > 100 W/cm^2 compared with undoped samples (0.1 W/cm^2). We propose that the origin of this increased stability is related to Bi migration that favors different reactions, leading to the formation first of BiI_3 and then to the stable bismuth oxyiodide compound (BiOI),[48] at the surface of the grains which hinders the usual decomposition mechanisms into PbI_2 and PbO_x in undoped $MAPbI_3$.

■ ASSOCIATED CONTENT

Supporting Information

The Supporting Information is available free of charge on the ACS Publications website at DOI: 10.1021/acs.chemmater.9b00270.

Details of (1) the synthesis of the Bi-doped films, (2) EDXFS data and composition of the samples, (3) XRD data and analysis, (4) optical absorption data and Tauc plots, (5) 770 nm PL evolution under irradiation of $MAPbI_3$, (6) NIR PL emission data and emission decay curves, (7) PL evolution under irradiation of Bi-doped $MAPbI_3$, (8) optical images of the transformation with temperature, (9) transformation of BiI_3 to BiOI, Raman spectra, and (10) EDX maps of irradiated regions (PDF)

■ AUTHOR INFORMATION

Corresponding Authors

*E-mail: ada@icmm.csic.es (A.d.A.)
*E-mail: carmen.coya@urjc.es (C.C.)

ORCID

Javier Bartolomé: 0000-0001-9407-6353
Alicia de Andrés: 0000-0003-4359-9001

Notes

The authors declare no competing financial interest.

■ ACKNOWLEDGMENTS

Funding by the Spanish Ministerio de Economía y Competitividad (MINECO) under Projects MAT2015-65356-C3-1-R, MAT2015-65356-C3-2-R, MAT2014-56607-R, and ENE2017-90565-REDT National Excellence Network is acknowledged. We also acknowledge MINECO for financial support and provision of synchrotron radiation facilities at the European Synchrotron Radiation Facility (ESRF) and thank Eduardo Salas for his assistance in using Spanish beamline BM25A SpLine at ESRF. J.B. acknowledges the funding from Comunidad de Madrid under the Talento fellowship 2017-T2/IND-5617.

DOI: 10.1021/acs.chemmater.9b00270
Chem. Mater. XXXX, XXX, XXX−XXX

REFERENCES

(1) Yang, W. S.; Noh, J. H.; Jeon, N. J.; Kim, Y. C.; Ryu, S.; Seo, J.; Seok, S. I. High-performance photovoltaic perovskite layers fabricated through intramolecular exchange. *Science* **2015**, *348*, 1234−1237.

(2) Green, M. A.; Hishikawa, Y.; Dunlop, E. D.; Levi, D. H.; Hohl-Ebinger, J.; Ho-Baillie, A. W. Y. Solar cell efficiency tables (version 52). *Prog. Photovoltaics* **2018**, *26*, 427−436.

(3) Sha, W. E. I.; Ren, X.; Chen, L.; Choy, W. C. H. The efficiency limit of $CH_3NH_3PbI_3$ perovskite solar cells. *Appl. Phys. Lett.* **2015**, *106*, 221104.

(4) Ginting, R. T.; Jeon, M.-K.; Lee, K.-J.; Jin, W.-Y.; Kim, T.-W.; Kang, J.-W. Degradation mechanism of planar-perovskite solar cells: correlating evolution of iodine distribution and photocurrent hysteresis. *J. Mater. Chem. A* **2017**, *5*, 4527−4534.

(5) Climent-Pascual, E.; Hames, B. C.; Moreno-Ramírez, J. S.; Álvarez, A. L.; Juarez-Perez, E. J.; Mas-Marza, E.; Mora-Seró, I.; de Andrés, A.; Coya, C. Influence of the substrate on the bulk properties of hybrid lead halide perovskite films. *J. Mater. Chem. A* **2016**, *4*, 18153−18163.

(6) Gracia, R. C.; Snodgrass, W. R. Lead toxicity and chelation therapy. *Am. J. Health-Syst. Pharm.* **2007**, *64*, 45−53.

(7) Peña, M. A.; Fierro, J. L. G. Chemical structures and performance of perovskite oxides. *Chem. Rev.* **2001**, *101*, 1981−2018.

(8) Stoumpos, C. C.; Malliakas, C. D.; Kanatzidis, M. G. Semiconducting Tin and Lead Iodide Perovskites with Organic Cations: Phase Transitions, High Mobilities, and Near-Infrared Photoluminescent Properties. *Inorg. Chem.* **2013**, *52*, 9019−9038.

(9) Hao, F.; Stoumpos, C. C.; Cao, D. H.; Chang, R. P. H.; Kanatzidis, M. G. Lead-free solid-state organic−inorganic halide perovskite solar cells. *Nat. Photonics* **2014**, *8*, 489−494.

(10) Mancini, A.; Quadrelli, P.; Milanese, C.; Patrini, M.; Guizzetti, G.; Malavasi, L. $CH_3NH_3Sn_xPb_{1-x}Br_3$ Hybrid Perovskite Solid Solution: Synthesis, Structure, and Optical Properties. *Inorg. Chem.* **2015**, *54*, 8893−8895.

(11) Klug, M. T.; Osherov, A.; Haghighirad, A. A.; Stranks, S. D.; Brown, P. R.; Bai, S.; Wang, J. T.-W.; Dang, X.; Bulović, V.; Snaith, H. J.; Belcher, A. M. Tailoring metal halide perovskites through metal substitution: influence on photovoltaic and material properties. *Energy Environ. Sci.* **2017**, *10*, 236−246.

(12) Lau, C. F. J.; Zhang, M.; Deng, X.; Zheng, J.; Bing, J.; Ma, Q.; Kim, J.; Hu, L.; Green, M. A.; Huang, S.; Ho-Baillie, A. Strontium-Doped Low-Temperature-Processed $CsPbI_2Br$ Perovskite Solar Cells. *ACS Energy Lett.* **2017**, *2*, 2319−2325.

(13) Hao, F.; Stoumpos, C. C.; Chang, R. P. H.; Kanatzidis, M. G. Anomalous Band Gap Behavior in Mixed Sn and Pb Perovskites Enables Broadening of Absorption Spectrum in Solar Cells. *J. Am. Chem. Soc.* **2014**, *136*, 8094−8099.

(14) Frolova, L. A.; Anokhin, D. V.; Gerasimov, K. L.; Dremova, N. N.; Troshin, P. A. Exploring the Effects of the Pb^{2+} Substitution in $MAPbI_3$ on the Photovoltaic Performance of the Hybrid Perovskite Solar Cells. *J. Phys. Chem. Lett.* **2016**, *7*, 4353−4357.

(15) Wang, R.; Zhang, X.; He, J.; Ma, C.; Xu, L.; Sheng, P.; Huang, F. Bi^{3+}-doped $CH_3NH_3PbI_3$: Red-shifting absorption edge and longer charge carrier lifetime. *J. Alloys Compd.* **2017**, *695*, 555−560.

(16) Zhou, Y.; Yong, Z.-J.; Zhang, K.-C.; Liu, B.-M.; Wang, Z.-W.; Hou, J.-S.; Fang, Y.-Z.; Zhou, Y.; Sun, H.-T.; Song, B. Ultrabroad Photoluminescence and Electroluminescence at New Wavelengths from Doped Organometal Halide Perovskites. *J. Phys. Chem. Lett.* **2016**, *7*, 2735−2741.

(17) Zhou, Y.; Yong, Z.-J.; Zhang, W.; Ma, J.-P.; Sadhanala, A.; Chen, Y.-M.; Liu, B.-M.; Zhou, Y.; Song, B.; Sun, H.-T. Ultra-broadband optical amplification at telecommunication wavelengths achieved by bismuth-activated lead iodide perovskites. *J. Mater. Chem. C* **2017**, *5*, 2591−2596.

(18) Slavney, A. H.; Hu, T.; Lindenberg, A. M.; Karunadasa, H. I. A Bismuth-Halide Double Perovskite with Long Carrier Recombination Lifetime for Photovoltaic Applications. *J. Am. Chem. Soc.* **2016**, *138*, 2138−2141.

(19) McClure, E. T.; Ball, M. R.; Windl, W.; Woodward, P. M. Cs_2AgBiX_6 (X = Br, Cl): New Visible Light Absorbing, Lead-Free Halide Perovskite Semiconductors. *Chem. Mater.* **2016**, *28*, 1348−1354.

(20) Park, B.-W.; Bertrand, P.; Xiaoliang, Z.; Håkan, R.; Gerrit, B.; Johansson, E. M. J. Bismuth Based Hybrid Perovskites $A_3Bi_2I_9$ (A: Methylammonium or Cesium) for Solar Cell Application. *Adv. Mater.* **2015**, *27*, 6806−6813.

(21) Hoye, R. L. Z.; Brandt, R. E.; Osherov, A.; Stevanović, V.; Stranks, S. D.; Wilson, M. W. B.; Kim, H.; Akey, A. J.; Perkins, J. D.; Kurchin, R. C.; Poindexter, J. R.; Wang, E. N.; Bawendi, M. G.; Bulović, V.; Buonassisi, T. Methylammonium Bismuth Iodide as a Lead-Free, Stable Hybrid Organic−Inorganic Solar Absorber. *Chem.—Eur. J.* **2016**, *22*, 2605−2610.

(22) Eckhardt, K.; Bon, V.; Getzschmann, J.; Grothe, J.; Wisser, F. M.; Kaskel, S. Crystallographic insights into $(CH_3NH_3)_3(Bi_2I_9)$: a new lead-free hybrid organic-inorganic material as a potential absorber for photovoltaics. *Chem. Commun.* **2016**, *52*, 3058−3060.

(23) Rodríguez-Carvajal, J.; Roisnel, T. FullProf Suite. https://www.ill.eu/sites/fullprof/index.html (accessed Feb 06, 2018).

(24) Solé, V. A.; Papillon, E.; Cotte, M.; Walter, P.; Susini, J. A multiplatform code for the analysis of energy-dispersive X-ray fluorescence spectra. *Spectrochim. Acta, Part B* **2007**, *62*, 63−68.

(25) Kamminga, M. E.; Stroppa, A.; Picozzi, S.; Chislov, M.; Zvereva, I. A.; Baas, J.; Meetsma, A.; Blake, G. R.; Palstra, T. T. M. Polar Nature of $(CH_3NH_3)_3Bi_2I_9$ Perovskite-Like Hybrids. *Inorg. Chem.* **2017**, *56*, 33−41.

(26) deQuilettes, D. W.; Zhang, W.; Burlakov, V. M.; Graham, D. J.; Leijtens, T.; Osherov, A.; Bulović, V.; Snaith, H. J.; Ginger, D. S.; Stranks, S. D. Photo-induced halide redistribution in organic−inorganic perovskite films. *Nat. Commun.* **2016**, *7*, 11683.

(27) Stranks, S. D.; Burlakov, V. M.; Leijtens, T.; Ball, J. M.; Goriely, A.; Snaith, H. J. Recombination Kinetics in Organic-Inorganic Perovskites: Excitons, Free Charge, and Subgap States. *Phys. Rev. Appl.* **2014**, *2*, 034007.

(28) Eames, C.; Frost, J. M.; Barnes, P. R. F.; O'Regan, B. C.; Walsh, A.; Islam, M. S. Ionic transport in hybrid lead iodide perovskite solar cells. *Nat. Commun.* **2015**, *6*, 7497.

(29) Shirayama, M.; Kadowaki, H.; Miyadera, T.; Sugita, T.; Tamakoshi, M.; Kato, M.; Fujiseki, T.; Murata, D.; Hara, S.; Murakami, T. N.; Fujimoto, S.; Chikamatsu, M.; Fujiwara, H. Optical Transitions in Hybrid Perovskite Solar Cells: Ellipsometry, Density Functional Theory, and Quantum Efficiency Analyses for $CH_3NH_3PbI_3$. *Phys. Rev. Appl.* **2016**, *5*, 014012.

(30) Meinert, M.; Günter, R. Electronic structure and optical band gap determination of $NiFe_2O_4$. *J. Phys.: Condens. Matter* **2014**, *26*, 115503.

(31) Kato, M.; Fujiseki, T.; Miyadera, T.; Sugita, T.; Fujimoto, S.; Tamakoshi, M.; Chikamatsu, M.; Fujiwara, H. Universal rules for visible-light absorption in hybrid perovskite materials. *J. Appl. Phys.* **2017**, *121*, 115501.

(32) Coya, C.; Ruiz, C.; Álvarez, Á. L.; Álvarez-García, S.; García-Frutos, E. M.; Gómez-Lor, B.; de Andrés, A. Star-shaped hexaaryltriindoles small molecules: Tuning molecular properties towards solution processed organic light emitting devices. *Org. Electron.* **2012**, *13*, 2138−2148.

(33) Leguy, A. M. A.; Azarhoosh, P.; Alonso, M. I.; Campoy-Quiles, M.; Weber, O. J.; Yao, J.; Bryant, D.; Weller, M. T.; Nelson, J.; Walsh, A.; van Schilfgaarde, M.; Barnes, P. R. F. Experimental and theoretical optical properties of methylammonium lead halide perovskites. *Nanoscale* **2016**, *8*, 6317−6327.

(34) de Quilettes, D. W.; Vorpahl, S. M.; Stranks, S. D.; Nagaoka, H.; Eperon, G. E.; Ziffer, M. E.; Snaith, H. J.; Ginger, D. S. Impact of microstructure on local carrier lifetime in perovskite solar cells. *Science* **2015**, *348*, 683−686.

(35) Yamada, Y.; Nakamura, T.; Endo, M.; Wakamiya, A.; Kanemitsu, Y. Photocarrier Recombination Dynamics in Perovskite $CH_3NH_3PbI_3$ for Solar Cell Applications. *J. Am. Chem. Soc.* **2014**, *136*, 11610−11613.

DOI: 10.1021/acs.chemmater.9b00270
Chem. Mater. XXXX, XXX, XXX−XXX

(36) Leijtens, T.; Stranks, S. D.; Eperon, G. E.; Lindblad, R.; Johansson, E. M. J.; McPherson, I. J.; Rensmo, H.; Ball, J. M.; Lee, M. M.; Snaith, H. J. Electronic Properties of Meso-Superstructured and Planar Organometal Halide Perovskite Films: Charge Trapping, Photodoping, and Carrier Mobility. *ACS Nano* **2014**, *8*, 7147−7155.
(37) Mosconi, E.; Merabet, B.; Meggiolaro, D.; Zaoui, A.; De Angelis, F. First-Principles Modeling of Bismuth Doping in the $MAPbI_3$ Perovskite. *J. Phys. Chem. C* **2018**, *122*, 14107−14112.
(38) Nayak, P. K.; Sendner, M.; Wenger, B.; Wang, Z.; Sharma, K.; Ramadan, A. J.; Lovrinčić, R.; Pucci, A.; Madhu, P. K.; Snaith, H. J. Impact of Bi^{3+} Heterovalent Doping in Organic−Inorganic Metal Halide Perovskite Crystals. *J. Am. Chem. Soc.* **2018**, *140*, 574−577.
(39) Milot, R. L.; Eperon, G. E.; Snaith, H. J.; Johnston, M. B.; Herz, L. M. Temperature-Dependent Charge-Carrier Dynamics in $CH_3NH_3PbI_3$ Perovskite Thin Films. *Adv. Funct. Mater.* **2015**, *25*, 6218−6227.
(40) Whitfield, P. S.; Herron, N.; Guise, W. E.; Page, K.; Cheng, Y. Q.; Milas, I.; Crawford, M. K. Structures, Phase Transitions and Tricritical Behavior of the Hybrid Perovskite Methyl Ammonium Lead Iodide. *Sci. Rep.* **2016**, *6*, 35685.
(41) Weller, M. T.; Weber, O. J.; Henry, P. F.; Di Pumpo, A. M.; Hansen, T. C. Complete structure and cation orientation in the perovskite photovoltaic methylammonium lead iodide between 100 and 352 K. *Chem. Commun.* **2015**, *51*, 4180−4183.
(42) Zaldo, C.; Solé, J. G.; Agulló-López, F. Study of the precipitation behavior of NaCl:Pb and KCl:Pb by optical spectroscopy. *J. Phys. Chem. Solids* **1982**, *43*, 837−844.
(43) Du, M.-H. Density Functional Calculations of Native Defects in $CH_3NH_3PbI_3$: Effects of Spin−Orbit Coupling and Self-Interaction Error. *J. Phys. Chem. Lett.* **2015**, *6*, 1461−1466.
(44) Duan, H.-S.; Zhou, H.; Chen, Q.; Sun, P.; Luo, S.; Song, T.-B.; Bob, B.; Yang, Y. The identification and characterization of defect states in hybrid organic-inorganic perovskite photovoltaics. *Phys. Chem. Chem. Phys.* **2015**, *17*, 112−116.
(45) Hamdeh, U. H.; Nelson, R. D.; Ryan, B. J.; Bhattacharjee, U.; Petrich, J. W.; Panthani, M. G. Solution-Processed BiI_3 Thin Films for Photovoltaic Applications: Improved Carrier Collection via Solvent Annealing. *Chem. Mater.* **2016**, *28*, 6567−6574.
(46) Evans, B. L. Optical properties of bismuth tri-iodide. *Proc. R. Soc. London, Ser. A* **1966**, *289*, 275−286.
(47) Fang, M.; Jia, H.; He, W.; Lei, Y.; Zhang, L.; Zheng, Z. Construction of flexible photoelectrochemical solar cells based on ordered nanostructural $BiOI/Bi_2S_3$ heterojunction films. *Phys. Chem. Chem. Phys.* **2015**, *17*, 13531−13538.
(48) Hoye, R. L. Z.; Lee, L. C.; Kurchin, R. C.; Huq, T. N.; Zhang, K. H. L.; Sponseller, M.; Nienhaus, L.; Brandt, R. E.; Jean, J.; Polizzotti, J. A.; Kursumović, A.; Bawendi, M. G.; Bulović, V.; Stevanović, V.; Buonassisi, T.; MacManus-Driscoll, J. L. Strongly Enhanced Photovoltaic Performance and Defect Physics of Air-Stable Bismuth Oxyiodide (BiOI). *Adv. Mater.* **2017**, *29*, 1702176.

DOI: 10.1021/acs.chemmater.9b00270
Chem. Mater. XXXX, XXX, XXX−XXX